



Cotterell, M. I., Mason, B. J., Carruthers, A. E., Walker, J. S., Orr-Ewing, A. J., & Reid, J. P. (2014). Measurements of the evaporation and hygroscopic response of single fine-mode aerosol particles using a Bessel beam optical trap. *Physical Chemistry Chemical Physics*, 16(5), 2118-2128.  
10.1039/c3cp54368d

Link to published version (if available):  
[10.1039/c3cp54368d](https://doi.org/10.1039/c3cp54368d)

[Link to publication record in Explore Bristol Research](#)  
PDF-document

## University of Bristol - Explore Bristol Research

### General rights

This document is made available in accordance with publisher policies. Please cite only the published version using the reference above. Full terms of use are available:  
<http://www.bristol.ac.uk/pure/about/ebr-terms.html>

### Take down policy

Explore Bristol Research is a digital archive and the intention is that deposited content should not be removed. However, if you believe that this version of the work breaches copyright law please contact [open-access@bristol.ac.uk](mailto:open-access@bristol.ac.uk) and include the following information in your message:

- Your contact details
- Bibliographic details for the item, including a URL
- An outline of the nature of the complaint

On receipt of your message the Open Access Team will immediately investigate your claim, make an initial judgement of the validity of the claim and, where appropriate, withdraw the item in question from public view.

# 1 Measurements of the Evaporation and Hygroscopic Response 2 of Single Fine-Mode Aerosol Particles Using a Bessel Beam 3 Optical Trap

4 *Michael I. Cotterell,<sup>1</sup> Bernard J. Mason,<sup>1</sup> Antonia E. Carruthers,<sup>2</sup> Jim S. Walker,<sup>1</sup> Andrew J. Orr-  
5 Ewing<sup>1</sup> and Jonathan P. Reid<sup>1</sup>*

6 <sup>1</sup> School of Chemistry, University of Bristol, Bristol, UK BS8 1TS

7 <sup>2</sup> School of Chemistry, Newcastle University, Newcastle Upon Tyne, UK NE1 7RU

8  
9 A single horizontally-propagating zeroth order Bessel laser beam with a counter-propagating gas flow  
10 was used to confine single fine-mode aerosol particles over extended periods of time, during which  
11 process measurements were performed. Particle sizes were measured by the analysis of the angular  
12 variation of light scattered at 532 nm by a particle in the Bessel beam, using either a probe beam at  
13 405 nm or 633 nm. The vapour pressures of glycerol and 1,2,6-hexanetriol particles were determined  
14 to be  $7.5 \pm 2.6$  mPa and  $0.20 \pm 0.02$  mPa respectively. The lower volatility of hexanetriol allowed better  
15 definition of the trapping environment relative humidity profile over the measurement time period,  
16 thus higher precision measurements were obtained compared to those for glycerol. The size evolution  
17 of a hexanetriol particle, as well as its refractive index at wavelengths 532 nm and 405 nm, were  
18 determined by modelling its position along the Bessel beam propagation length while collecting phase  
19 functions with the 405 nm probe beam. Measurements of the hygroscopic growth of sodium chloride  
20 and ammonium sulfate have been performed on particles as small as 350 nm in radius, with growth  
21 curves well described by widely used equilibrium state models. These are the smallest particles for  
22 which single-particle hygroscopicity has been measured and represent the first measurements of  
23 hygroscopicity on fine mode and near-accumulation mode aerosols, the size regimes bearing the most  
24 atmospheric relevance in terms of loading, light extinction and scattering. Finally, the technique is  
25 contrasted with other single particle and ensemble methods, and limitations are assessed.

26

## 27 **I. Introduction**

28 Atmospheric aerosols play important roles in regulating the Earth's climate and influencing  
29 atmospheric composition, as well as impacting on human health, yet many of the fundamental  
30 physicochemical properties of aerosol remain poorly understood and quantified.<sup>1</sup> As well as their  
31 ability to scatter solar radiation directly, atmospheric aerosols indirectly affect climate by providing  
32 cloud condensation nuclei (CCN) for cloud droplets, impacting on the size, composition and lifetime  
33 of clouds.<sup>1,2</sup> Understanding the condensational growth of an aerosol and the partitioning of water  
34 between the gas and particle phases is critical to describe accurately the size distribution and  
35 composition of atmospheric aerosol.<sup>3</sup> Measurements of the response of the equilibrium particle size  
36 and composition to changes in relative humidity (RH) can be used to quantify the hygroscopicity of  
37 the aerosol, the capacity of a particle to absorb water from the surrounding vapour.<sup>4-7</sup> Further,  
38 changes in the partitioning of volatile and semi-volatile solutes (organic and inorganic) between the  
39 particle and gas phases can accompany changes in the RH.<sup>8</sup> Measurements of the decreasing radius of  
40 a particle evaporating into a gas phase devoid of the volatile or semi-volatile component can allow  
41 the vapour pressure of the component to be determined.<sup>9-11</sup>

42  
43 Ensemble measurements have been used extensively to probe aerosol systems in the fine ( $< 2.5 \mu\text{m}$   
44 diameter) and accumulation ( $0.1 - 1 \mu\text{m}$ ) mode regimes, providing measurements of quantities  
45 averaged over a large number of particles with insufficient resolution to quantify aerosol processes  
46 robustly at the fundamental level of individual particles. Single particle techniques can be employed  
47 successfully in the measurement of aerosol optical and thermodynamic properties, as well as their  
48 kinetic response, and have the potential to resolve the fundamental detail of physicochemical  
49 processes.<sup>11</sup> The use of electrodynamic balances (EDBs) to isolate and study single particles is well  
50 established, with recent improvements in experimental techniques allowing highly accurate  
51 measurements of particle hygroscopicity, but has been largely limited to studying coarse mode  
52 particles  $> 5 \mu\text{m}$  in radius.<sup>9,4</sup> Optical tweezers are routinely used to isolate and study aerosol particles  
53  $1 - 10 \mu\text{m}$  in radius, still much larger than the accumulation mode particles that are of direct  
54 atmospheric importance.<sup>12,13,2,14</sup> Thus, the size regimes examined by ensemble and single-particle

55 techniques do not overlap; there is a need for new techniques to control and characterise individual  
56 fine mode particles in order to reconcile single particle and ensemble measurements.

57

58 The need for single aerosol particle studies in the fine mode is augmented by the fact that some  
59 significant and atmospherically-relevant aerosol processes occur for diameters well below 1 micron.  
60 For example, the Kelvin equation shows that the vapour pressure for semi-volatile organic aerosol  
61 (SVOA) increases exponentially as the particle radius decreases (and the surface curvature  
62 increases).<sup>15</sup> However, the influence of the Kelvin effect is negligible for the coarse mode particles  
63 that are probed in existing single particle techniques. Although measurements of the kinetics of  
64 aerosol transformation (for example, heterogeneous oxidative aging or water condensation/  
65 evaporation) can be made routinely on single coarse mode particles, the accuracy of scaling the  
66 observed kinetics to the much smaller fine mode particles found in the atmosphere is frequently  
67 debated.<sup>11</sup> Further, and of particular relevance for the direct influence of aerosol on climate, particle  
68 diameters in the range 500 nm to 1  $\mu\text{m}$  are of sufficiently high number concentration and optical  
69 cross-section to play a significant role in atmospheric optics. Direct measurements of aerosol optical  
70 properties in this size range would be particularly advantageous. Single particle techniques that can  
71 access the fine mode and push the lower size limit down well into the accumulation mode would  
72 expand the range of particle sizes accessible to single particle techniques and allow the robust  
73 assessment and development of thermodynamic, kinetic and optical models.

74

75 A carefully engineered Bessel laser beam<sup>16,17</sup> may be used as an optical trap for single, as well as  
76 multiple, aerosol particles across a range of particle sizes, from 10s of microns to a few hundred  
77 nanometres in diameter.<sup>18-20</sup> The intensity profile along the transverse direction (*i.e.* in the direction  
78 perpendicular to the optical propagation axis) of a zeroth order Bessel beam (BB) is circularly  
79 symmetric with a central core of intensity surrounded by multiple rings. It can be shown by Fourier  
80 optics that such a beam is realisable by propagating the wave vectors of an incident beam along a  
81 cone, which may be achieved using a conical-shaped lens, or *axicon*.<sup>21-24</sup> The axicon method  
82 generates a BB over an extended distance due to the large region over which waves may interfere. If

83 an imaging plane is placed at any point along this interference region, a Bessel-squared intensity  
84 distribution is observed. Crucially, the core of a BB appears *non-diffracting* and retains its size and  
85 shape over a macroscopic length far larger than the characteristic Rayleigh range of a Gaussian beam  
86 with the same focal beam waist as the BB core diameter.<sup>16</sup> If a particle is irradiated by the core of a  
87 BB, it will experience radiation pressure force in the direction of the propagation axis of the beam,  
88 while optical gradient forces act in the transverse directions to retain the particle within the core. To  
89 confine single particles along the BB propagation length, the radiation pressure force needs to be  
90 balanced. If two counter-propagating BBs are used, a radiation pressure trap is created in which the  
91 trapping of both spherical and non-spherical sub-micron particles over macroscopic distances may be  
92 achieved.<sup>18</sup>

93  
94 Previous work has shown that BBs can be used to trap and characterise multiple aerosol particles 500  
95 to 2000 nm in radius, with their sizes resolved from the angular variation of elastically scattered  
96 light.<sup>18,19</sup> We have previously shown that the accuracy of such sizing methods can be enhanced by  
97 sizing with multiple-wavelength probe beams, which is particularly valuable for determinations of  
98 size for particles below 1 micron in radius. Furthermore, the size range of particles trapped by the  
99 beam can be coarsely tuned by varying the core size and laser power of the BB, and may be  
100 optimised for trapping fine mode particles. More recently, we have reported the use of a vertically  
101 propagating BB optical trap coupled with cavity ring-down spectroscopy to measure directly the  
102 optical extinction by single aerosol particles<sup>20</sup>

103  
104 The purpose of this paper is to demonstrate that BBs can be used to study the physiochemical  
105 properties of fine mode aerosols over extended periods of time. A single horizontally propagating BB  
106 is coupled with a counter-propagating gas flow to balance the radiation pressure force exerted on  
107 confined aerosol particles. This arrangement allows the environment around a single particle to be  
108 varied easily without perturbing the trapping stability. Measurements of particle hygroscopicity and  
109 gas-particle partitioning of semi-volatile components are reported.

110

## 111 **II. Experimental Description**

112 The experimental apparatus used is summarised in Figure 1. A 532 nm Gaussian laser beam (Laser  
113 Quantum 3W Opus) was expanded using a pair of lenses (L1 and L2) to illuminate the back-aperture  
114 of a 2° axicon (Altechna), generating a region of interference of approximately one meter in length  
115 over which a BB was formed. Immediately after the axicon, the BB core diameter was measured to  
116 be 55  $\mu\text{m}$ , which is too large to trap sub-micron aerosols. Hence, a further pair of lenses (L3 and L4)  
117 was used to reduce the core diameter by a factor of 12.5 times to  $4.7 \pm 0.3 \mu\text{m}$ , propagating over a  
118 distance of approximately 5 mm. This beam was directed into the trapping cell. The radiation  
119 pressure exerted by this horizontally propagating BB on a trapped particle was balanced by a  
120 humidified nitrogen gas flow of 50 sccm, the RH of which could be controlled. This gas flow was  
121 also used to purge the cell of excess aerosol. The speed of the gas flow combined with the geometry  
122 of the trapping cell yields a Reynolds number  $Re$  close to 1, much lower than the critical value for  $Re$   
123 of approximately 3000 for turbulent flow. The RH inside the trapping cell was monitored using a  
124 capacitance probe (Honeywell). A camera (C1) coupled to a 20 $\times$  long working distance objective  
125 with a numerical aperture (NA) of 0.42 was used to capture the phase function from a single trapped  
126 aerosol,<sup>25,19</sup> while a second camera (C2) coupled to a 10 $\times$  objective tracked the position of the particle  
127 along the full propagation length of the BB. C2 also indicated whether multiple particles were  
128 trapped. Aerosol was introduced into the cell via a medical nebuliser (Omron). If multiple particles  
129 were trapped, the trapping cell was evacuated and fresh aerosol was nebulised into the cell. This  
130 process was repeated until only a single particle was trapped.

131

132 Aerosol radii typically have dimensions on the order of the wavelength of visible light. Semi-  
133 empirical models cannot describe the angular variation in the light scattering intensity, the phase  
134 function (PF), and Mie theory must instead be used. The elastic scattering intensity distribution is  
135 affected not only by particle radius but also by the polarisation of the incident light and the refractive  
136 index (RI) of the particle,  $m$ . Here, we denote the real and imaginary components of the RI by  $n$  and  $k$   
137 respectively. Measuring the angular variation in the scattered intensity and simulating the measured  
138 distribution using Mie theory provides a method of obtaining the particle size even for sub-micron

139 aerosol particles.<sup>26</sup> This simulation is obtained by computing a library of Mie PFs, comparing each  
140 one with the measured PF and performing a least-squares fit. The library of PFs can be computed by  
141 floating the variables of particle radius and RI. Typically, for a single measured PF there may be  
142 multiple fit solutions with different values of radius for different RI values. Thus, in our  
143 measurements, the RI is modelled using literature data and only the radius is fitted.

144

145 In addition to the recorded PFs at 532 nm from elastically scattered light from the BB, two further  
146 probe beams of different wavelength were employed. The first was from a 35 mW 405 nm diode laser  
147 (IQ Series, Power Technology Incorporated) and the second was from a 2 mW 633 nm HeNe laser  
148 (LHP073, Melles Griot). These additional probe beams were combined using a polarisation beam  
149 splitter (PBS) and aligned anti-parallel to the BB direction. The probe beams were gently focussed  
150 into the trapping plane using a 400 mm lens (L5) in order to obtain sufficient scattered light for  
151 detection by C1, although their irradiances in the trapping plane were low enough not to affect the  
152 particles position and considerably less than that from the trapping 532 nm laser. When collecting  
153 PFs from the additional probe beams, various band pass filters were placed between the objective and  
154 CCD in C1 to allow collection of light from the respective probe beams and block the more intense  
155 532 nm scattered light from the BB.

156

### 157 **III. Measurements of Component Vapour Pressures**

158 Volatilities (vapour pressures) of organic compounds are key thermodynamic properties required for  
159 quantifying semi-volatile organic aerosol (SVOA).<sup>27</sup> Vapour pressures can be estimated from single  
160 particle measurements by recording the change in radius over time. Glycerol is a good benchmark  
161 system to estimate the validity of the BB approach for studying aerosol volatilities; the relatively low  
162 hygroscopicity means glycerol absorbs little water, so may be assumed to have a well-defined  
163 composition. Numerous glycerol droplets were studied using the BB apparatus, collecting the time-  
164 dependent PFs as a droplet was allowed to evaporate. Note that for these experiments, PFs were only  
165 collected at 532 nm.

166

167 Dry nitrogen was flowed into the trapping cell at a flow rate of 50 sccm until the in-cell RH probe  
 168 reported a stable, low RH, typically between 5 – 10 %. When an aqueous glycerol solution was  
 169 nebulised into the cell, the in-cell RH increased rapidly to 25 – 30 % before returning to a stable 5 –  
 170 10 % after 6 - 8 minutes. Because of the small size of the droplets (less than 2  $\mu\text{m}$ ) and their fast  
 171 evaporation (under 15 minutes), leaving the measured RH to equilibrate and stabilise at low RH  
 172 before data acquisition was not possible. However, the low hygroscopicity of glycerol (particularly  
 173 when compared with inorganic salt systems) suggests the non-zero and varying RH will have a  
 174 negligible effect on the particle size and evaporation profile. When fitting PFs to Mie theory  
 175 simulations, the RI was assumed to be constant and equal to the pure component value of  $m = 1.475 +$   
 176  $i 10^{-8}$  over the entire experiment.<sup>28</sup> Maxwell-Garnett and volume-weighting mixing rules show that  
 177 the difference in the real component of the RI at 0 % and 20 % RH is 0.012, a 0.8 % deviation. This  
 178 corresponds to a 0.8 % difference in the Mie theory fit radius, which is of a similar magnitude to the  
 179 uncertainties in PF measurements of radius. Other sources of uncertainty include noise in the PF  
 180 measurements, not using a precise angular range, and from not using plane wave illumination of the  
 181 particle, which is a fundamental assumption of Mie scattering theory.

182

183 Figure 2(a) shows the radius changes observed for four glycerol particles as they evaporate over time.  
 184 One measurement is for a coarse mode particle of  $\sim 2.9 \mu\text{m}$  in radius, evaporating to a radius of  $\sim 1.7$   
 185  $\mu\text{m}$ . Further data sets show that fine mode glycerol particles may be trapped and characterised, with  
 186 one particle evaporating from a radius of  $\sim 800 \text{ nm}$  to 500 nm. Droplet vapour pressures,  $p$ , may be  
 187 obtained by fitting the Maxwell equation (1) to the time-dependent data.<sup>11</sup>

$$188 \quad \frac{da^2}{dt} = \frac{2D_{ij}M_i}{R\rho} \left( \frac{p_\infty}{T_\infty} - \frac{p}{T} \right) \quad (1)$$

189  $D_{ij}$  is the gas diffusion coefficient of species  $i$  in the surrounding phase  $j$ ,  $M_i$  is the molecular weight,  
 190  $a$  is the particle radius,  $R$  is the molar gas coefficient,  $\rho$  is the density,  $p$  and  $p_\infty$  are the vapour  
 191 pressures at the droplet surface and at infinite distance from the droplet respectively, and  $T$  and  $T_\infty$  are  
 192 the corresponding temperatures, assumed to be the same in this case for slow evaporation of low



193 volatility components. By taking the vapour pressure of component  $i$  at infinite distance to be  
194 negligible and including the effect of non-zero RH, equation (2) can be derived where  $m_i$  is the mass  
195 fraction of solute  $i$ .

$$196 \quad \frac{da^2}{dt} = -\frac{2D_{ij}M_i p}{R\rho T m_i} \quad (2)$$

197 Because of non-ideality in the interactions between different species, the pure component vapour  
198 pressure,  $p_0$ , is related to the measured vapour pressure by  $p = p_0\gamma_i x_i$ , where  $\gamma_i$  is the activity  
199 coefficient and  $x_i$  is the mole fraction of species  $i$  in the droplet. Hence, by plotting the radius-  
200 squared as a function of time, a straight-line fit should be achieved where the gradient is related to  $p_0$ .  
201 Figure 2(b) summarises the result of measuring 11 pure component vapour pressures in this way,  
202 having assumed that both the activity coefficient and the mole fraction of glycerol are equal to unity.  
203 The average glycerol vapour pressure is  $7.5 \pm 2.6$  mPa, agreeing satisfactorily with the literature  
204 value of 11.6 mPa.<sup>29,28</sup> This level of agreement is quite reasonable when the more significant  
205 variations in vapour pressure determinations for components with similar vapour pressures such as  
206 dicarboxylic acids are considered.<sup>11</sup> It will now be shown that the wide variation in the measured  
207 vapour pressures for glycerol droplets is primarily due to the large variation in the in-cell RH at the  
208 beginning of droplet evaporation, and the relatively high volatility of glycerol.

209  
210 One difficulty in calculating a precise vapour pressure for glycerol is in determining an accurate  
211 measure of the RH surrounding the glycerol particles. Nebulising aerosol into the trapping cell causes  
212 a large increase in the in-cell RH. Ideally, following nebulisation and particle trapping, the cell would  
213 be left for ~20 minutes, passing dry N<sub>2</sub> gas into the cell until the RH stabilises at low (5 – 10 %) RH.  
214 1,2,6-Hexanetriol droplets evaporate more slowly than glycerol, owing to the much lower vapour  
215 pressure of the triol and so more accurate measurements of vapour pressure might be expected.  
216 Hence, multiple hexanetriol droplets were studied using the BB apparatus. The measurements were  
217 performed at an average RH in the range 5 – 10 %, with an RH profile that was more stable than for  
218 the previous glycerol studies. Unlike the glycerol experiments, PFs were instead collected at 405 nm

219 while still employing the 532 nm BB for optical trapping, allowing us to investigate simultaneously  
220 the accuracy with which an unknown RI can be determined. Here, we show that the quasi-equilibrium  
221 variation in position of hexanetriol droplets along the length of the BB ( $\lambda = 532$  nm), observed  
222 experimentally using camera C2 (Figure 1), can be modelled by Mie theory to obtain both the size  
223 evolution of the particle and the RI at 532 nm. Once the size evolution of the particle is determined,  
224 the PFs ( $\lambda = 405$  nm) collected with camera C1 are then fitted, while varying the RI at 405 nm so as  
225 to give the same size evolution as given by modelling of the positional data. Thus, these  
226 measurements yield simultaneously particle size and refractive index at two wavelengths.

227

228 In aerosol optical tweezers, where particles are typically 2 – 10  $\mu\text{m}$  in radius, Raman spectroscopy is  
229 used to determine simultaneously radius and refractive index with high accuracy.<sup>25</sup> Whispering  
230 gallery modes (WGMs) superimposed on spontaneous Raman bands arise because certain frequencies  
231 couple efficiently with the resonant modes of droplet microcavities. However, this method of size  
232 determination cannot be employed when probing single particles in the fine mode as there are too few  
233 WGMs within the Raman bandwidth for reliable size analysis. A Raman spectrum is a form of  
234 *resonance spectrum*, which traditionally describes scattering intensity as a function of the size  
235 parameter, the ratio of the circumference of a spherical particle to the incident wavelength. Measuring  
236 scattering intensity variation with size at a fixed angle is an alternative method of obtaining a  
237 resonance spectrum. For example, Ray and co-workers measured resonances in the scattering  
238 intensity for an evaporating glycerol droplet.<sup>30</sup> The position of a confined particle along the length of  
239 the core of a BB when subjected to a counter-propagating gas flow is highly dependent on the  
240 radiation pressure efficiency of a particle and, as we will show, follows the form of a typical  
241 resonance spectrum. Thus, measuring the relative position of an evaporating particle along the length  
242 of a BB provides an alternative method of deriving the size evolution of a particle and can be  
243 exploited even for sub-micron aerosol particles.

244

245 The position of a particle along a single Bessel beam with a counter-propagating gas flow depends on  
246 two forces: (i) the force exerted by the laser beam through the action of radiation pressure ( $F_{pr}$ ); (ii)

247 the Stokes drag force exerted by the gas flow. While the Stokes drag force is simply dependent on the  
248 gas flow velocity and particle radius,  $F_{pr}$  is more complicated and is proportional to the product of the  
249 on-axis core intensity and the radiation pressure efficiency,  $Q_{pr}$ , of the particle. The latter term is a  
250 measure of how efficiently and asymmetrically a particle scatters light; a particle back-scattering a  
251 higher fraction of light has a higher  $Q_{pr}$  value.<sup>31</sup> Figure 3(a) shows the variation in position of a  
252 hexanetriol particle along the length of the single BB optical trap as a function of evaporation time.  
253 The sharp resonances in positional data directly correspond to the resonance structures in  $Q_{pr}$  and  
254 occur at unique sizes. Hence, only Mie theory simulations of  $Q_{pr}$  are required to derive the size  
255 evolution of a particle and the effects of Stokes drag and variations in the BB core intensity can be  
256 neglected.

257

258 The procedure for comparing positional data with Mie simulations to retrieve droplet size is similar to  
259 the fitting of Mie resonance spectra in previous single particle measurements by Chylek *et al.*<sup>32-34</sup> and  
260 Ray *et al.*<sup>30,35</sup>, and is now briefly described.  $Q_{pr}$  is simulated as a function of particle radius and  
261 repeated for fixed single values of RI over a range of RIs. Sharp resonance peaks in the  $Q_{pr}$   
262 simulations (in the radius domain) can be assigned by matching to peaks in the positional data (which  
263 are obtained in the time domain), while also ensuring that the underlying contour reflecting higher  
264 order Mie terms is consistent with the data. Plotting these assigned radii against their respective times  
265 of observation gives the size evolution of the particle, connecting time, the particle radius, and its  
266 position along the length of the BB.

267

268 Figure 3(b) shows the correspondence between the resonant sizes in  $Q_{pr}$  and the resonant excursions  
269 in the particle position along the length of the BB. Differences in the signal amplitude between the  
270 positional data and the  $Q_{pr}$  simulations are likely because the effects of Stokes drag and variations in  
271 the core intensity with propagation have been neglected. It can be seen in Figure 3(b) that the  
272 positions of resonance peaks in the position data do not agree exactly with the positions of resonance  
273 peaks in the  $Q_{pr}$  simulation. The residual differences between the positions of resonance peaks in the

274 Mie simulation ( $a_{i,sim}$ ) and the experimental measurement ( $a_{i,exp}$ ) provide a measure of the  
275 agreement between the simulation (for a given RI) and the position measurements. The total residual  
276 of a fit,  $D_{fit}$ , is given by equation (3).

$$277 \quad D_{fit} = \sum_i |a_{i,exp} - a_{i,sim}| \quad (3)$$

278 Repeating this procedure and obtaining the fit residuals for simulations using different RIs allows a  
279 determination of the RI at 532 nm. This outcome is demonstrated in Figure 3(c) for three studies,  
280 which indicate an RI of  $1.482 \pm 0.001$  at 532 nm. Refractometer measurements give a bulk refractive  
281 index of 1.4758 at a wavelength of 589.6 nm. A higher refractive index at a lower wavelength is  
282 expected, given typical trends in dispersion for other materials. No literature data at the wavelength  
283 of 532 nm can be found.

284

285 Figure 4(a) shows how the radii evolve with time for five droplets, with droplet sizes determined from  
286 their positional data as well as from their 405 nm PF data. When performing the PF analysis, the RI at  
287 405 nm was adjusted until only the initial radius (i.e. the radius at  $t = 0$  s) matched that given from  
288 modelling the positional data. Subsequent trends during evaporation illustrate the consistency that is  
289 then obtained between the two size-determination methods at the two wavelengths. Assuming the  
290 imaginary component of the RI,  $k$ , to be equal to  $10^{-8}$ , the real component,  $n$ , at 405 nm was  
291 consistently determined to be  $1.485 \pm 0.006$  from measurements on multiple droplets. Again, no  
292 literature value of RI can be found specifically at the wavelength of 405 nm which to compare our  
293 measured value. The three real RIs now obtained for hexanetriol (1.485 at 405 nm, 1.482 at 532 nm,  
294 1.476 at 589.6 nm) can be fitted to refractive index models such as Cauchy's equation. RI's at further  
295 wavelengths are required to quantitatively assess the accuracy of such models in describing the  
296 dispersion in the RI of hexanetriol. The possibility of retrieving a more detailed wavelength  
297 dependence of RI will feature in future work.

298

299 The five hexanetriol droplets remained optically trapped for much longer than glycerol droplets, with  
300 one droplet isolated for 10 hours. As experiments were performed at a low RH of  $\sim 5\%$ , the mass

301 fraction of water in the droplets is assumed to be negligible and the activity coefficient of hexanetriol  
302 is taken to be unity. Figure 4(b) shows calculated vapour pressures for five droplets with an average  
303 value of  $0.20 \pm 0.02$  mPa. The 10% variation in the measured hexanetriol  $p_0$  compared to the 35%  
304 variation for glycerol demonstrates that greater reproducibility can be achieved in vapour pressure  
305 measurements when the in-cell RH can be well defined. No comment can be made on the accuracy of  
306 our measurement of  $p_0$  for hexanetriol as there are no current literature values for this compound with  
307 which to compare.

308

#### 309 **IV. Hygroscopic Growth Measurements**

310 Hygroscopicity studies require measurements of the changes in the equilibrium partitioning of water  
311 between the gas and particle phases with variation in RH, most often through measurements of  
312 relative size.<sup>11</sup> Due to non-ideal interaction of water with solutes, thermodynamic models are required  
313 to describe the activity coefficients of solutions, particularly for the supersaturated droplets probed in  
314 aerosol systems. Here, we compare hygroscopic growth measurements of involatile inorganic salt  
315 systems to simulations of growth from the Extended Aerosol Inorganic Model (E-AIM), an  
316 equilibrium state model which can describe the relationship between particle growth and changes in  
317 the RH.<sup>36</sup> Vapour pressure and hygroscopicity measurements aid in the parameterisation and  
318 validation of such thermodynamic models.<sup>11</sup>

319

320 As an aerosol particle takes up water with an increase in RH, both the RI and size of the particle  
321 change. Fitting the PFs obtained from binary component droplets (water and solute) in hygroscopicity  
322 experiments is more complicated than fitting those from vapour pressure experiments and it is not  
323 possible to retrieve both the RI and size from a single PF, with several solution combinations of RI  
324 and particle radius possible. Instead, the RI has to be described as a function of particle radius,  $a$ . For  
325 a binary system with volume fractions  $\varphi_1$  and  $\varphi_2$  for pure water and pure solute, respectively, the  
326 linear volume-fraction average mixing rule is often encountered in studies of aerosols. However, this  
327 treatment of refractive index is not applicable in many cases, as shown by Liu and Daum.<sup>37</sup> Thus, we

328 have opted to use the parameterisations of Tang and Munkelwitz<sup>38</sup> for various inorganic aerosol  
 329 systems, which is now briefly described. The real component of the RI,  $n$ , for a binary aerosol can be  
 330 modelled in terms of particle radius,  $a$ , using equation (4).

$$331 \quad n = n_w + gc_2 + hc_2^2 = n_w + g \left[ \frac{a_0^3 c_{2,0}}{a^3} \right] + h \left[ \frac{a_0^3 c_{2,0}}{a^3} \right]^2 \quad (4)$$

332  $n_w$  is the real component of RI for pure water,  $c_2$  is the solute concentration, and  $a_0$  is the particle  
 333 radius at some reference concentration of solute  $c_{2,0}$ . Tang and Munkelwitz<sup>38</sup> reported the RIs at 633  
 334 nm of several aqueous inorganic aerosols and their dependence on the solute concentration,  $c_2$ . Using  
 335 their parameterisations, the constants  $g$  and  $h$  in equation (4) may be calculated for a particular  
 336 inorganic species. Figure 5 shows the variation of  $n$  with  $c_2$  for both a sodium chloride and an  
 337 ammonium sulphate aerosol, as determined by Tang and Munkelwitz. A polynomial fit to their  
 338 parameterisation gives the constants  $g$  and  $h$ . A small wavelength correction is also applied to the RI  
 339 to account for dispersion; we use the correction given by Millard and Seaver.<sup>39</sup> The parameters  
 340  $c_{2,0}$  and  $a_0$  remain to be determined. The E-AIM model can relate RH to solute concentration, so  
 341 using the measurement of the in-cell RH (which has a  $\pm 2\%$  accuracy) E-AIM is used to determine the  
 342 solute concentration  $c_{2,0}$  at a reference RH (usually taken to be the RH at  $t = 0$  s). Subsequently,  
 343 equation (4) is used to determine the RI of the initial droplet at  $c_{2,0}$ . The PF recorded at this reference  
 344 RH is then fitted using this value of RI to determine  $a_0$ . A library of phase functions can now be  
 345 generated in the same way as in previous PF analyses, except that the RI is varied with radius in the  
 346 form given by equation (5), as opposed to having a constant value.

347

348 Aqueous sodium chloride droplets were nebulised into the optical trapping cell and the initial RH was  
 349 kept high (between 85 – 95 %). The laser power was set at powers in the range 1 – 2 W,  
 350 corresponding to core intensities in the range 0.3 - 0.6 mW  $\mu\text{m}^{-2}$ . After an equilibration time of ~20  
 351 minutes, the RH was lowered to 30-40% over 1 hour, during which time the particle axial positions  
 352 along the propagation distance and the PFs at 532 nm were recorded. The changes in RH are

353 sufficiently slow that the droplet is always at equilibrium during measurement and, thus, water  
354 transport kinetics can be neglected. An example data set is shown in Figure 6(a). As expected, the  
355 particle radius decreases as the in-cell RH is reduced and effloresces in the region 37 – 41 % RH (for  
356 comparison, literature values range from 39 to 54% RH).<sup>11</sup> Unlike in optical tweezers experiments,  
357 the effloresced particle remains stably trapped. Predictions of the radial growth factor (RGF)  
358 calculated from the E-AIM model can be compared to the pre-efflorescence data. The RGF is the ratio  
359 of the particle radius to its radius at 0% RH (dry radius). E-AIM calculations of RGF were fitted to  
360 the experimental data using a least-squares method and floating the dry radius parameter. The  
361 distribution of normalised least-squares residuals with dry radius can be fitted to a Gaussian  
362 distribution, from which an uncertainty in the dry radius can be obtained. This uncertainty is shown in  
363 Figure 6(a) by the shaded grey area. The experimental pre-efflorescence data show good agreement  
364 with E-AIM, and the dry radius obtained by the fit is indicated by the dashed red line.

365  
366 Interestingly, the PFs from the supposedly crystalline NaCl particle closely resemble those expected  
367 from a sphere, with distinct dark and bright fringes, although they were observed to ‘shimmer’ at  
368 times with bright fringes appearing broken in a regular pattern. The fact that a PF resembling a  
369 spherical particle is obtained may suggest that the effloresced NaCl particle has not adopted the  
370 expected equilibrium cubic structure immediately. Modelling post-efflorescence PFs with Mie theory  
371 gives dry particle radii very close to the values expected from the E-AIM fit to the pre-efflorescence  
372 data. This is shown by the experimental data points in Figure 6(a) distributed just below the dashed  
373 red line, implying the PFs obtained are indeed for an effloresced NaCl particle but for a period during  
374 which the effloresced particle remains approximately spherical. Although effloresced NaCl particles  
375 are generally assumed to have a cubic shape, nearly spherical NaCl particles have been observed by  
376 others in the literature.<sup>40</sup>

377  
378 Further information is given by the particle position data along the propagation length of the BB  
379 (Figure 6(b)). The pattern of periodic resonances expected for a particle that is changing size ends  
380 after efflorescence, as marked in the figure by the label ‘crystallisation’. However, position

381 fluctuations continue following efflorescence, but are seemingly random in nature. The reason for  
382 these fluctuations is unclear. One possibility is that the effloresced particle is not completely  
383 crystalline and initially retains at least some of the solution phase. This structure may be evolving  
384 over time, tending towards the equilibrium cubic structure of NaCl as further residual water  
385 evaporates from the particle. Such structural changes will impact on the optical properties and  
386 radiation pressure efficiency of a particle, affecting its position along the length of the BB.  
387 Instantaneous fluctuations in the orientation of the particle in the optical trap as it tumbles, if non-  
388 spherical, can also lead to large and rapid deviations in particle position as the magnitude of the  
389 radiation pressure changes.

390

391 So far, the particles studied are far larger than the fine mode particles we wish to probe using Bessel  
392 beams. Carruthers and co-workers showed that the size range of particles isolated using BB optical  
393 traps can be preferentially selected by changing the BB core diameter.<sup>19</sup> Thus, reducing the core  
394 diameter should favour the trapping of smaller particles. The post-axicon BB core diameter was  $55.5$   
395  $\pm 2.9$   $\mu\text{m}$  and may be tuned in the optical trapping region by tweaking the focal length ratio of lenses  
396 L3 to L4 in Figure 1. The lens ratio L3/L4 was increased to 20 from the value of 12.5 used so far,  
397 resulting in the measured core diameter decreasing from  $4.7 \pm 0.3$   $\mu\text{m}$  to  $2.6 \pm 0.1$   $\mu\text{m}$ . Also, the solute  
398 concentration in the nebuliser can be reduced so as to produce a size distribution of nebulised aerosol  
399 peaking at smaller size. Subsequent hygroscopicity studies performed on aqueous NaCl droplets  
400 clearly showed the trapping and reliable sizing of NaCl droplets down to radii of 600 nm, with the  
401 hygroscopic growth curves again broadly consistent with predictions from E-AIM. Smaller particles  
402 were optically trapped, but their PFs recorded at 532 nm were featureless so the particles could not be  
403 sized.

404

405 In an attempt to size aerosol truly within the fine mode reliably, use of a lower (visible) probe  
406 wavelength is logical. To this end, the 35 mW 405 nm probe beam (alignment as shown in Figure 1)  
407 was used to collect PFs. Figure 7 shows an example of a hygroscopicity measurement for an aqueous



408 NaCl droplet, using the 405 nm probe beam to determine the radius for a droplet which could not be  
409 reliably sized using the 532 nm beam. The figure also shows the corresponding PFs at 405 nm and  
410 532 nm for the droplet at  $t = 0$  s (corresponding to 80 % RH). The 405 nm PF clearly has features  
411 which can be used to fit to Mie theory simulations, whereas the 532 nm PFs are completely  
412 featureless (neglecting the side peaks from optical aberrations). The radius of the droplet was  
413 determined to be 510 nm from the PF at the probe wavelength of 405 nm. Droplets have been reliably  
414 sized down to radii of  $\sim 350$  nm, well into the fine mode regime relevant to atmospheric chemistry and  
415 physics. These results represent the smallest single-particle measurements of hygroscopicity made.  
416 Indeed, particles around this size present the largest total optical cross-section to visible light in the  
417 atmosphere, with large geometric cross-section, extinction and scattering efficiency and sufficient  
418 number density.

419

420 Ammonium sulfate is another atmospherically-relevant aerosol system and hygroscopicity  
421 measurements have been performed using the BB apparatus, measuring PFs using the 405 nm probe  
422 beam. A summary plot, averaging the RGF from hygroscopic growth measurements of seven  
423 accumulation mode droplets ( $< 500$  nm in radius), is presented in Figure 8(a). Errors are calculated by  
424 taking the standard deviation in the RGF values, and assuming a  $\pm 2$  % standard error in the measured  
425 RH. Figure 8(b) also shows a summary of seven studies on sodium chloride accumulation mode  
426 particles. Evidently, for both ammonium sulfate and sodium chloride, the hygroscopic growth of  
427 accumulation mode particles is well described by E-AIM.

428

## 429 **V. Conclusions**

430 The capability of BB optical traps to measure the vapour pressure and hygroscopicities of fine and  
431 accumulation mode aerosol has been successfully demonstrated. Vapour pressures of organic aerosol  
432 have been measured, with a demonstrated reproducibility within 16 % precision if the optical trapping  
433 cell RH can be well defined and maintained over the entire course of the experiment. A first attempt  
434 has been presented to model the position of particles subjected to radiation pressure from the BB and

435 a counter-propagating gas flow. Analysis of the sharp resonances in particle position data determines  
436 both the size evolution of hexanetriol particles and the RI at 532 nm. The accuracy of the RI value  
437 obtained is limited by the resolution of the position of the particle along the length of the beam. This  
438 uncertainty can be reduced by using a longer BB core length and by reducing the exposure on the  
439 camera recording the particle position giving higher time resolution of particle position. The size  
440 evolution of the particle from position data agrees with that determined by analysis of PFs recorded  
441 using a 405 nm probe beam. This agreement is only achieved when using a fixed real component of  
442 the RI at 405 nm of  $1.485 \pm 0.006$ . Future work will involve repeating measurements for further probe  
443 beam wavelengths (e.g. 633 nm) to see how well dispersion models describe the wavelength  
444 dependence of the RI of hexanetriol.

445

446 Hygroscopicity measurements on sodium chloride and ammonium sulfate aerosols have been  
447 performed for particles as small as 350 nm in radius. These results represent the first single-particle  
448 measurements of hygroscopicity on fine mode and accumulation mode aerosols, the size regime  
449 which has the most atmospheric significance in terms of loading and light extinction/scattering  
450 efficiencies. The variation in radial growth factor with RH agrees well with the results from the E-  
451 AIM thermodynamic models. There are two principal factors that raise questions over the reliability  
452 of our measurements. Firstly, the RH within the cell is poorly defined with a precision of  $\pm 2\%$  at  
453 best. It is further assumed that the in-cell RH measured by a probe near to the wall of the cell is the  
454 same as that experienced by an optically trapped particle at the centre of the trapping cell. We have  
455 attempted to ensure that this is true by positioning the RH probe as close to the trapping region as  
456 possible given the physical constraints of the trapping cell. If the probe is saturated there could be a  
457 delay in equilibration of the probe with the environment of the rest of the cell. Secondly, the fitting of  
458 PFs relies on having an accurate description of the RI and assumes a dependence on radius. Although  
459 the parameterisations of Tang and Munkelwitz<sup>38</sup> are commonly used to describe RI as a function of  
460 concentration, we have to use our measurements of RH to obtain the starting droplet concentration,  
461 which suffers from an uncertainty of  $\pm 2\%$ . Further, Tang and Munkelwitz's parameterisations are

462 valid at 633 nm only. So, when describing the RI of sodium chloride or ammonium sulfate for PFs  
463 recorded from a 405 nm probe beam, a dispersion model formulated for sea salt aerosol is applied.<sup>39</sup>  
464 However, such dispersion models may not be valid over such large wavelength ranges.

465

466 EDB techniques are now at a point at which the RH of the trapping cell can be defined to better than  
467 0.2 %.<sup>4</sup> However, EDB methods also employ PF analysis to extract size information so they still rely  
468 on modelling the RI. As well as being able to extract aerosol radius to a precision better than 1 nm,  
469 optical tweezers methods employing Raman spectroscopy can simultaneously measure the RI with an  
470 uncertainty better than 0.1 %, and can quantify the dispersion over a narrow wavelength range.<sup>12</sup>  
471 However, RH measurements are performed by capacitance probe methods so suffer the same level of  
472 uncertainty as our measurements. Thus, to exploit the high level of accuracy in quantifying droplet  
473 size and RI in such measurements, comparative measurements on multiple droplets must be  
474 performed.<sup>41</sup> Indeed, we have shown here that the uncertainty with which hygroscopic growth  
475 measurements can be made on fine mode inorganic aerosol using the BB optical trapping approach ( $\pm$   
476 3% error in RGF for a given RH) is comparable to the typical uncertainty associated with ensemble  
477 accumulation mode measurements made using the hygroscopic tandem differential mobility analysis  
478 technique, typically  $\pm$  3% for inorganic aerosol as seen in Figure 1 of reference <sup>42</sup> with errors in RH  
479 that are also similar.

480

#### 481 **Acknowledgements**

482 JPR, AJOE and AEC acknowledge financial support from the EPSRC through the support of a  
483 Leadership Fellowship (EP/G007713/1) awarded to JPR. MIC acknowledges funding from NERC and  
484 the RSC through an Analytical Trust Fund studentship award and support from the Aerosol Society in  
485 the form of a CN Davies award. BJM and JSW acknowledge the EPSRC for funding. We also  
486 acknowledge Thomas C. Preston for helpful discussions.

487

488 **References**

- 489 1. S. Solomon, D. Qin, M. Manning, M. Marquis, K. Averyt, M. M. B. Tignor, J. Miller, Henry  
 490 LeRoy, and Z. Chen, *Climate Change 2007: The Physical Science Basis - Contribution of*  
 491 *Working Group I to the Fourth Assessment Report of the Intergovernmental Panel on Climate*  
 492 *Change*, 2007.
- 493 2. G. McFiggans, et al., *Atmos. Chem. Phys.*, 2006, **6**, 2593–2649.
- 494 3. J. Julin, M. Shiraiwa, R. E. H. Miles, J. P. Reid, U. Pöschl, and I. Riipinen, *The Journal of*  
 495 *Physical Chemistry A*, 2013, **117**, 410–20.
- 496 4. J. F. Davies, A. E. Haddrell, A. M. J. Rickards, and J. P. Reid, *Anal. Chem.*, 2013, **85**, 5819–  
 497 5826.
- 498 5. D. A. Hegg, D. S. Covert, K. K. Crahan, H. H. Jonsson, and Y. Liu, *Geophysical Research*  
 499 *Letters*, 2006, **33**, L21808.
- 500 6. B. J. Mason, S.-J. King, R. E. H. Miles, K. M. Manfred, A. M. J. Rickards, J. Kim, J. P. Reid,  
 501 and A. J. Orr-Ewing, *The Journal of Physical Chemistry. A*, 2012, **116**, 8547–8556.
- 502 7. A. R. Attwood and M. E. Greenslade, *The Journal of Physical Chemistry A*, 2012, **116**, 4518–  
 503 4527.
- 504 8. D. Topping, P. Connolly, and G. McFiggans, *Nature Geoscience*, 2013, **6**, 443–446.
- 505 9. J. F. Davies, A. E. Haddrell, and J. P. Reid, *Aerosol Science and Technology*, 2012, **46**, 37–41.
- 506 10. F. D. Pope, H. Tong, B. J. Dennis-smither, P. T. Griffiths, S. L. Clegg, J. P. Reid, and R. A.  
 507 Cox, *The Journal of Physical Chemistry A*, 2010, **114**, 10156–10165.
- 508 11. U. K. Krieger, C. Marcolli, and J. P. Reid, *Chemical Society Reviews*, 2012, **41**, 6631–62.
- 509 12. R. E. H. Miles, J. S. Walker, D. R. Burnham, and J. P. Reid, *Physical Chemistry Chemical*  
 510 *Physics*, 2012, **14**, 3037–47.
- 511 13. B. J. Dennis-Smith, K. L. Hanford, N.-O. A. Kwamena, R. E. H. Miles, and J. P. Reid, *The*  
 512 *Journal of Physical Chemistry. A*, 2012, **116**, 6159–68.
- 513 14. R. M. Power, S. H. Simpson, J. P. Reid, and A. J. Hudson, *Chemical Science*, 2013, **4**, 2597–  
 514 2604.
- 515 15. E. R. Lewis, *Journal of Aerosol Science*, 2006, **37**, 1605–1617.
- 516 16. J. Durnin, *Journal of the Optical Society of America A*, 1987, **4**, 651–654.
- 517 17. J. Durnin and J. J. Miceli, *Physical Review Letters*, 1987, **58**, 1499–1501.
- 518 18. A. E. Carruthers, J. P. Reid, and A. J. Orr-Ewing, *Optics Express*, 2010, **18**, 14238–44.
- 519 19. A. E. Carruthers, J. S. Walker, A. Casey, A. J. Orr-Ewing, and J. P. Reid, *Phys. Chem. Chem.*  
 520 *Phys.*, 2012, **14**, 6741–6748.

- 521 20. J. S. Walker, A. E. Carruthers, A. J. Orr-Ewing, and J. P. Reid, *The Journal of Physical*  
522 *Chemistry Letters*, 2013, **4**, 1748–1752.
- 523 21. D. McGloin and K. Dholakia, *Contemporary Physics*, 2005, **46**, 15–28.
- 524 22. M. Duocastella and C. B. Arnold, *Laser & Photonics Reviews*, 2012, **6**, 607–621.
- 525 23. J. Jezek, T. Cizmár, V. Nedela, and P. Zemánek, *Optics express*, 2006, **14**, 8506–15.
- 526 24. M. Mazilu, D. J. Stevenson, F. Gunn-Moore, and K. Dholakia, *Laser & Photonics Reviews*,  
527 2009, **4**, 529–547.
- 528 25. R. E. H. Miles, A. E. Carruthers, and J. P. Reid, *Laser & Photonics Reviews*, 2011, **5**, 534–  
529 552.
- 530 26. J. P. Reid and L. Mitchem, *Annual Review of Physical Chemistry*, 2006, **57**, 245–71.
- 531 27. I. Riipinen, I. K. Koponen, A. Hyva, J. Vanhanen, H. Lihavainen, K. E. J. Lehtinen, M. Bilde,  
532 and M. Kulmala, *The Journal of Physical Chemistry. A*, 2007, **111**, 12995–13002.
- 533 28. H. K. Cammenga, F. W. Schulze, and W. Theuerl, *Journal of Chemical and Engineering Data*,  
534 1977, **22**, 131–134.
- 535 29. J. F. Davies, A. E. Haddrell, and J. P. Reid, *Aerosol Science and Technology*, 2012, **46**, 666–  
536 677.
- 537 30. A. K. Ray, R. Johnson, and A. Souyri, *Langmuir*, 1989, **5**, 133–140.
- 538 31. W. M. Irvine, *Journal of the Optical Society of America*, 1965, **55**, 16–21.
- 539 32. P. Chýlek, *Journal of the Optical Society of America*, 1976, **66**, 285–287.
- 540 33. P. Chylek, J. T. Kiehl, and M. K. W. Ko, *Physical Review A*, 1978, **18**, 2229–2233.
- 541 34. P. Chylek, V. Ramaswamy, A. Ashkin, and J. M. Dziedzic, *Applied Optics*, 1983, **22**, 2302–  
542 2307.
- 543 35. A. K. Ray, A. Souyri, E. J. Davis, and T. M. Allen, *Applied Optics*, 1991, **30**, 3974–3983.
- 544 36. S. L. Clegg, P. Brimblecombe, and A. S. Wexler, *The Journal of Physical Chemistry A*, 1998,  
545 **102**, 2155–2171.
- 546 37. Y. Liu and P. H. Daum, *Journal of Aerosol Science*, 2008, **39**, 974–986.
- 547 38. I. N. Tang and H. R. Munkelwitz, *Journal of Geophysical Research*, 1994, 18801–18808.
- 548 39. R. C. Millard and G. Seaver, *Deep-Sea Research*, 1990, **37**, 1909–1926.
- 549 40. A. Zelenyuk, Y. Cai, and D. Imre, *Aerosol Science and Technology*, 2006, **40**, 197–217.
- 550 41. J. S. Walker, J. B. Wills, J. P. Reid, L. Wang, D. O. Topping, J. R. Butler, and Y.-H. Zhang,  
551 *The Journal of Physical Chemistry. A*, 2010, **114**, 12682–91.

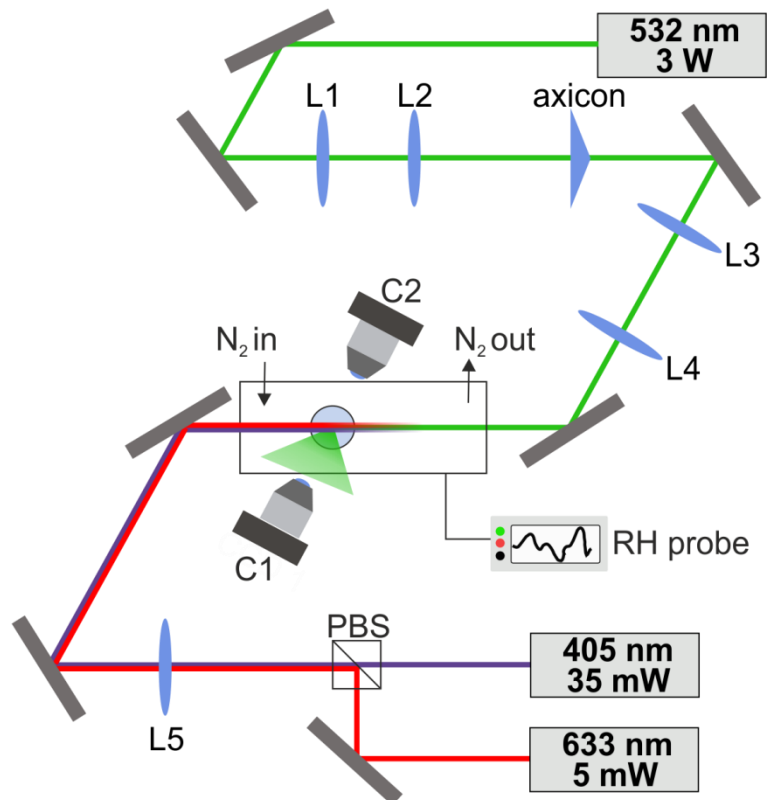
552 42. N. Good, D. O. Topping, J. Duplissy, M. Gysel, N. K. Meyer, A. Metzger, S. F. Turner, U.  
553 Baltensperger, Z. Ristovski, E. Weingartner, H. Coe, and G. McFiggans, *Atmospheric*  
554 *Chemistry and Physics Discussions*, 2010, **10**, 2577–2593.

555

556

557

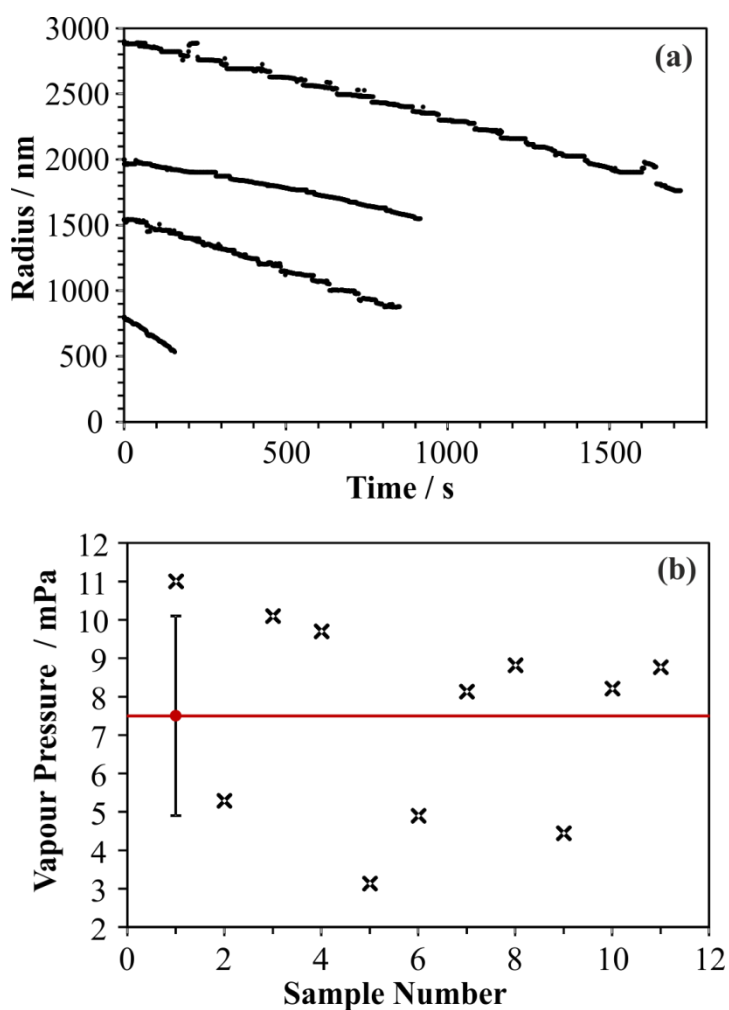
558 **Figure 1 – Schematic of the apparatus used to generate a Bessel beam and optically trap single aerosol particles. C1**  
559 **and C2 represent ‘camera 1’ and ‘camera 2’ respectively, PBS is a ‘polarisation beam splitter’, and L1-L5 represent**  
560 **lenses.**



561

562

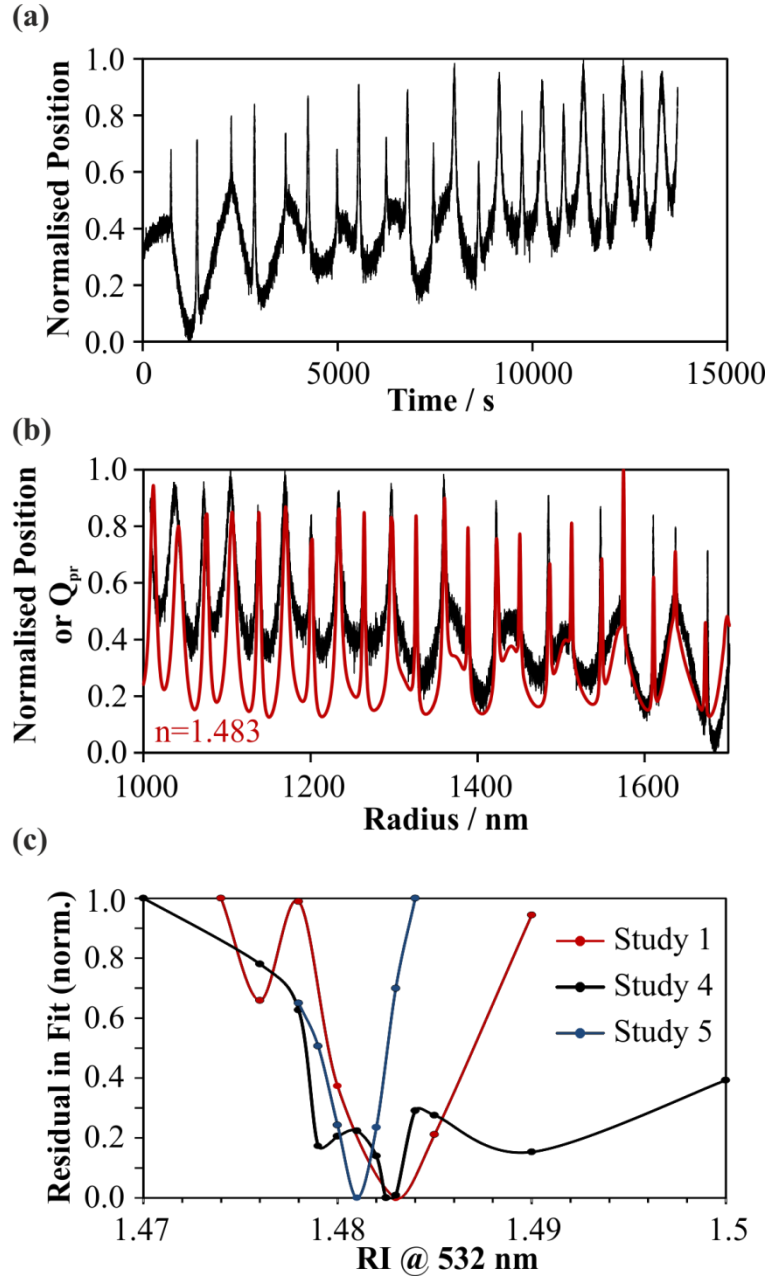
563 Figure 2 - (a) Four data sets measuring the radius as a function of time for optically-trapped glycerol droplets as they  
564 evaporate at an RH of ~15-20 %. (b) Vapour pressures from eleven studies give an average  $p_0$  of  $7.5 \pm 2.6$  mPa. The  
565 crosses indicate individual measurements and the circle and error bar indicate the mean and standard deviation.



566  
567

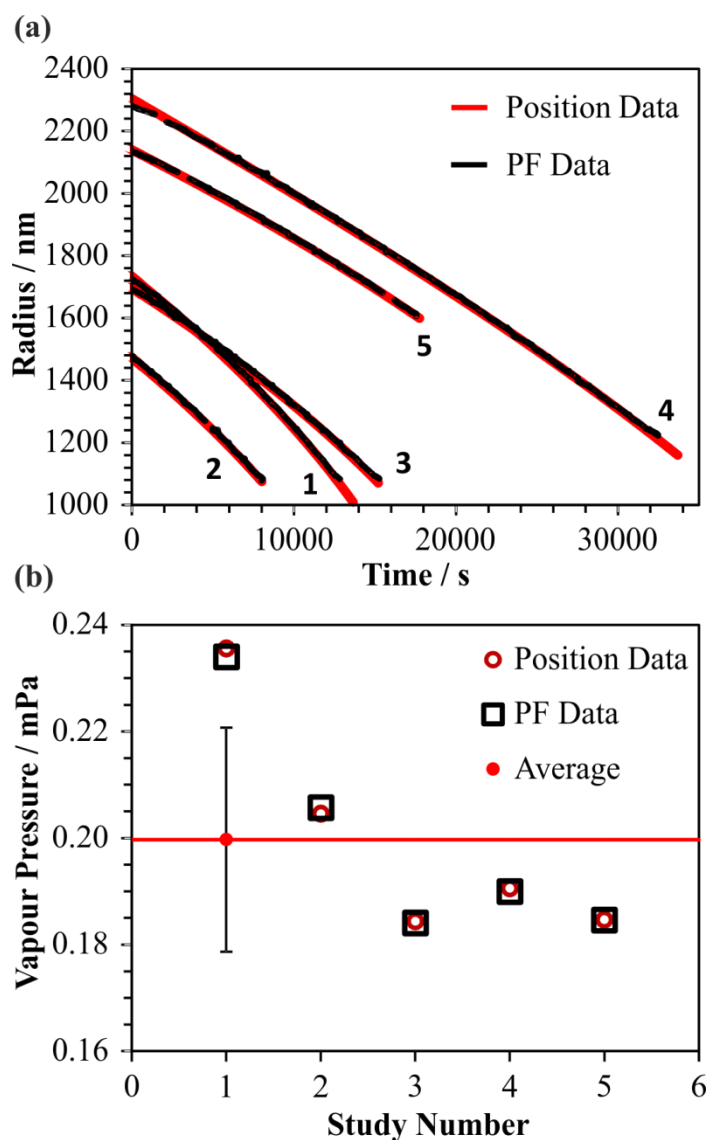


568 Figure 3 – (a) Measured position of the hexanetriol droplet in Study 1 along the length of a Bessel beam as it  
 569 evaporates over time. (b) Measured position data from Study 1 (black) in the radius domain, accompanied by the best  
 570 fit simulation of  $Q_{pr}$  (red) which used a real component of the RI of 1.483. (c) Normalised residual in  $Q_{pr}$  fits as a  
 571 function of RI at 532 nm for three different studies. Lines between data points are to guide the eye only.



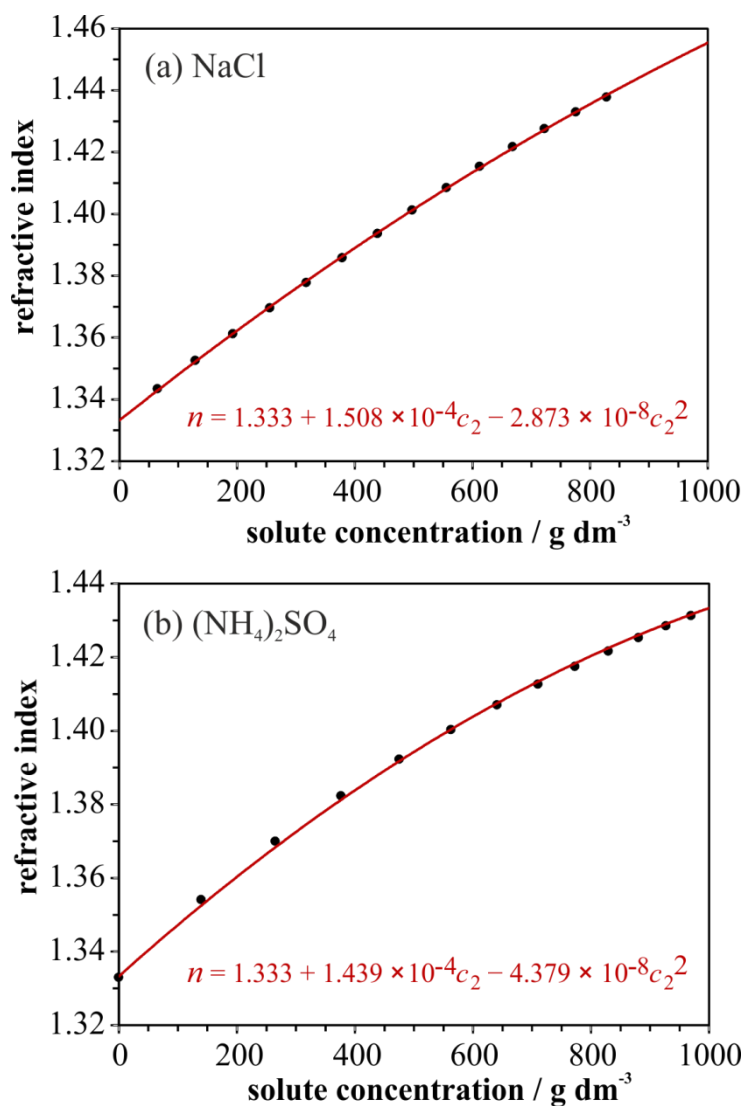
572  
 573

574 Figure 4 - (a) Five hexanetriol studies measuring the radius as a function of time using position data (red) and  
 575 subsequent measurement from phase function data (black). (b) Vapour pressures from five hexanetriol studies give  
 576 an average  $p_0$  of  $0.20 \pm 0.02$  mPa.



577  
 578

579 Figure 5 – The calculated variation in the real component of refractive index,  $n$ , with solute concentration,  $c_2$ , using  
580 the parameterisations of Tang and Munkelwitz.<sup>38</sup> Black dots show data points, while the red line is a second-order  
581 polynomial fit to data points, the equation for which is given.

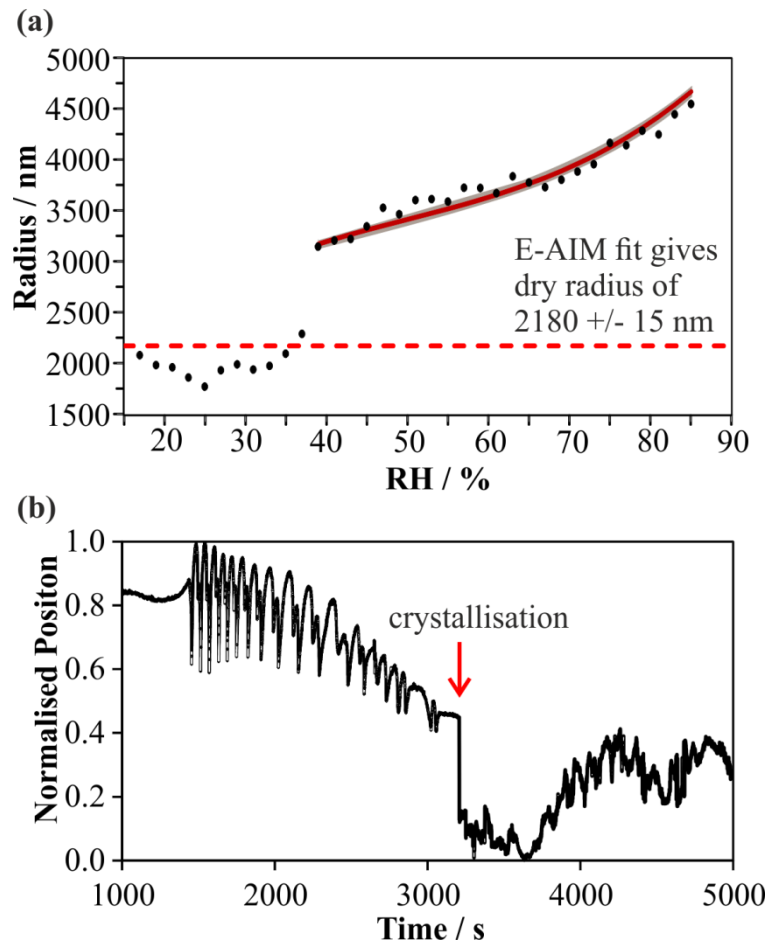


582

583

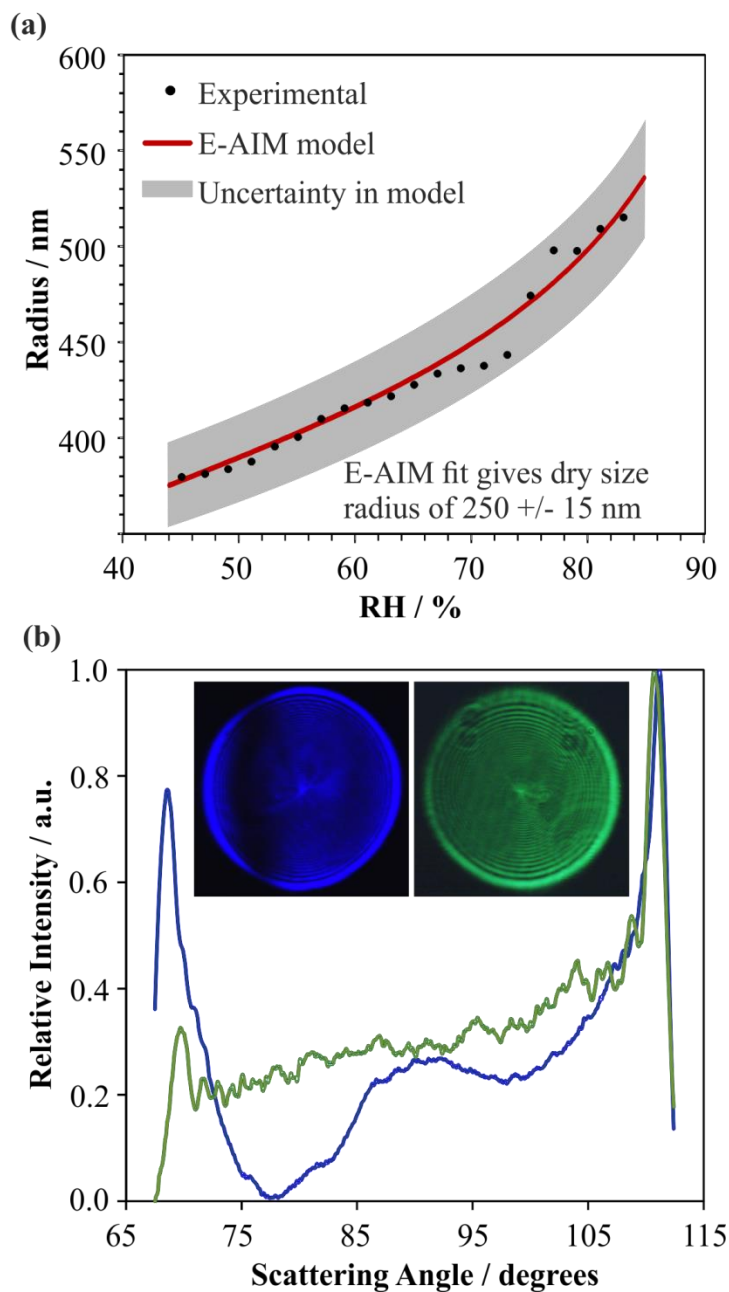
584

585 Figure 6 – (a) An example NaCl hygroscopicity data set using a 4.7  $\mu\text{m}$  core diameter Bessel beam. Experimental data  
586 points shown by black dots, accompanied by a comparison to the E-AIM model (red line) which has an associated  
587 uncertainty (shaded grey area). Dashed red line indicates the dry radius estimated from a fit of E-AIM model to  
588 experimental data points. Typical uncertainty in relative humidity is  $\pm 2\%$ . (b) The particle position along the Bessel  
589 beam length for the data set in (a).



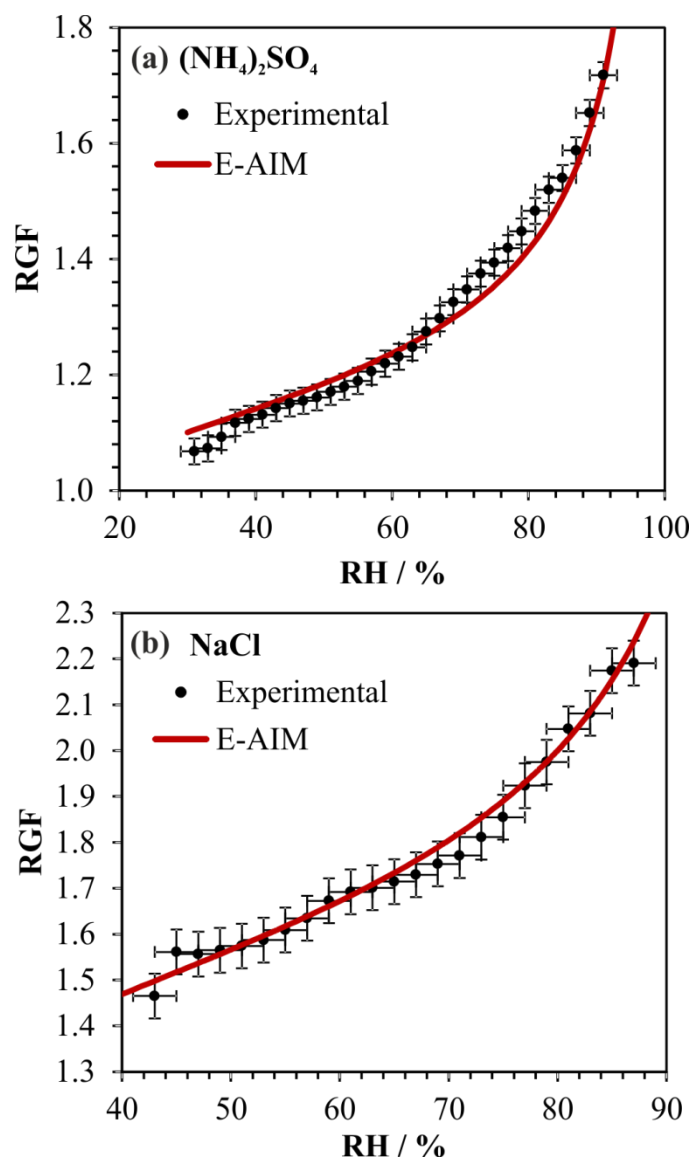
590  
591

592 Figure 7 – (a) Example hygroscopicity study on an aqueous NaCl aerosol droplet in the accumulation mode regime,  
593 with the radius determined from 405 nm phase functions. (b) Phase functions at probe wavelengths 405 nm (blue line)  
594 and 532 nm (green line) for the initial droplet in (a) at high relative humidity. Inset are the raw phase function images  
595 at 405 nm and 532 nm.



596  
597

598 Figure 8 – Summary of hygroscopic growth measurements on: (a) ammonium sulfate; (b) sodium chloride. In each  
599 case, the radial growth factor is an average from seven hygroscopic growth measurements on accumulation mode  
600 (<500 nm radius) aerosol particles.



601